Messung elektromagnetischer Kaskaden und der von ihnen erzeugten Neutronen bei 6,3 GeV (Measurements on Electromagnetic Cascades at 6.3 Gev Energies, and Subsequently Produced Neutrons) by G.Bathow, E. Freytag and K. Tesch. (DESY Report 66/13,) May 1966. 2 Hamburg 52. Notkestieg 1. Translated from the German (July 1966) by R.C.Klewe.

TRANSLATED FOR
STANFORD LINEAR ACCELERATOR CENTER

**********

# MEASUREMENTS ON ELECTROMAGNETIC CASCADES AT 6.3 Gev ENERGIES, AND SUBSEQUENTLY PRODUCED NEUTRONS

by

G.Bathow, E. Freytag and K.Tesch

## Summary

The electromagnetic cascades produced by 6.3 Gev bremsstrahlung in lead, copper and heavy concrete have been measured by means of an ionization chamber, The measured transition curves are compared with existing Monte Carlo calculations; data useful for shielding calculations are given. Neutrons produced by the cascades are measured by activation foils in several energy ranges, the results are compared with estimates. The angular distributions of the neutrons and in some cases their attenuation by the material are presented.

## 1. Introduction

Whereas most experiments in high-energy physics deal with the interaction of individual particles, measurements on cascades consider the total interaction of a beam of particles with a block of compact material. These experiments have two main purposes, either comparison of experimental results with earlier theoretical calculations, or the collection of data for shielding evaluations.

If the incident beam of particles is either electrons or $\gamma$ rays, the particles produced in the compact medium can be divided into two types, according to their interactions: electrons or $\gamma$-quanta, representing the electromagnetic cascade, and strongly interacting particles, the results of photoproduction, which go on to produce further particles by nuclear processes.

Measurements of electromagnetic cascades have been made by various methods, using ionization chambers[1], scintillation counters[2], photographic emulsions[3], spark chambers[4], cloud chambers[5-7], Čerenkov counters[8], bubble chambers[9], and thermo-luminescent crystals[10]. The above papers, apart from the high-energy work in ref. 5, deal

with the energy range up to 1 Gev. The present paper describes measurements made on electromagnetic cascades produced in lead, copper, and heavy concrete by 6.3 Gev bremsstrahlung. In the cases of lead and copper the experimental results could be compared with explicit Monte-Carlo calculations for the longitudinal and lateral development of the cascade[11]. Heavy concrete is of interest for shielding purposes. The measurements were made with an ionization chamber in a target formed of a stack of plates of the particular material.

Many papers have appeared on the possible individual processes whereby strongly interacting particles are produced by photons, but no measurements are available on photoproduction through electromagnetic cascades. One is therefore forced to resort to estimates from cascade theory[13] (see also ref. 12). Measurements were therefore carried out using nuclear emulsion plates and activated films, which would throw light on the production and subsequent scattering of neutrons (and protons) of various energy ranges. These measurements were made both in the stacks used in the cascade determinations, and

also in thick targets. The neutron and proton components of the radiation are of particular interest in shielding problems. The results obtained from the nuclear emulsion plates will not be presented in this paper because the evaluations now carried out by C. Passow*, K. Heinze**, and L. Hoffmann*** are still in progress.

## 2. Experimental Layout

The Y rays used in the experiment were produced by 6.3 Gev electrons from the synchrotron striking an internal tantalum target plate 0.5 mm thick. About 22 m from the target was a lead collimator 1 cm in diameter, followed by a magnet to remove charged particles from the Y ray beam. The beam remained in vacuum within the synchrotron ring and while it was led through the shielding wall into the experimental hall, but passed through air in the hall itself.

The experimental layout is shown in Figure 1.

---

* Institute of Experimental Nuclear Physics, Karlsruhe.

** Industrial Association for Radiation Protection, Technische Hochschule, Hannover.

*** CERN, Geneva.

The thin-walled ionization chamber (wall thickness $2 \times 10^{-4}$ radiation lengths) served as a beam monitor and was calibrated before each measurement against the quantum counter. Since the ionization chamber was also sensitive to the synchrotron radiation of accelerating particles, this had to be eliminated using 2 mm thick lead sheet in front of the collimator.

The entire region was shielded by concrete walls, and was covered over with concrete slabs.

## 3. Measurement of the electromagnetic cascade

### 3.1 Method

Measurement of the particle density at a given depth of material and the rate of energy loss, and in particular the lateral distribution, enables cascade calculations to be checked. These values can be derived from the degree of ionization in an ionization chamber using the Bragg-Gray principle[17]. Since the calculations assume an infinitely narrow beam, a very accurately collimated beam must be used in the experiments. The focusing of the cascade at 6 Gev is very strong, so that the lateral flux density gradient is

very high. To measure this lateral distribution, the detector must not be moved in either a slit or hole, but must always be shielded from the axis of the cascade by material, so that any side-scattered particles are immediately reabsorbed.

The detector must be made sufficiently small to be able to measure the flux gradient, and also sufficiently thin so that any differences in its critical energy with respect to the material being studied do not introduce distortions into the cascade[16].

Measurement of the dose rate in air behind a specific thickness of material, or else in a probe cavity, yields information concerning shielding calculations in which the absorption rate in tissue, or as an approximation in air, is required rather than a particle flux.

Ideally, one would use an ionization chamber whose wall thickness was known to be equivalent to the depth of tissue being investigated. Also, the incident beam must have a diameter that is commonly used in practice.

Measurements were made between the plates of the stack of the material being examined with a small plexiglass ionization chamber (30 $mm^3$ in volume, wall thickness $4 \times 10^{-3}$ radiation lengths, air-filled). These gave data useful for shielding calculations, and enabled a comparison to be made with existing Monte-Carlo calculations. The lateral distribution thus obtained does not allow, for the reasons given above, a direct comparison with theoretical distributions. However, the chamber is sufficiently small to give the longitudinal distribution of the cascade, calculated by integrating across the lateral distribution between each plate*. Since the chamber is not made of the material being investigated, (particularly difficult in the case of concrete) it is not possible to calculate the rate of energy deposition with the aid of the Bragg-Gray principle. Instead, the longitudinal distribution must be so normalised that its integral is equal to the total incident energy. On the other hand, the plexiglass chamber used gives dose values important for shielding calculations.

---

* It is planned to measure the true lateral distribution with luminescent glass using a different experimental layout.

At greater distances from the beam axis a more sensitive chamber 1 $cm^3$ in volume was used. The distance of the chamber from the axis could be changed by remote control. The stack of plates consisted of 40 x 40 $cm^2$ sheets hanging closely one after the other. Immediately in front of the stack there was a 20 cm long lead collimator with a 40 mm aperture. Table 1 shows the thickness of plates used, and also the values used for the radiation lengths $X_o$ (ref. 14). The composition of the concrete is given in Table 2.

Table 1. Decay coefficients of the electromagnetic cascade in various stacks. $\lambda_{min}$ and $X_o$ for concrete were calculated from its composition

| Material | Radiation length $X_o$ (cm) | Sheet thickness (cm) | Sheet thickness ($X_o$) | $\lambda_{min}$ ($cm^{-1}$) | $\lambda_{cascade}$ ($cm^{-1}$) | $\lambda(0^o)$ ($cm^{-1}$) |
|---|---|---|---|---|---|---|
| Lead | 0.56 | 0.5 | 0.89 | 0.47 | 0.49 | 0.1 |
| Copper | 1.45 | 0.8 | 0.55 | 0.27 | 0.25 | 0.27 |
| Heavy concrete ($C_p$ = 3.7 g/$cm^3$) | 5.0 | 5.0 | 1.00 | 0.091 | 0.070 | 0.09 |

Table 2. Composition of the heavy concrete

| Element | Fraction by weight |
|---|---|
| H | 0.004 |
| O | 0.344 |
| Mg | 0.019 |
| Al | 0.010 |
| Si | 0.060 |
| Ca | 0.048 |
| Mn | 0.001 |
| Fe | 0.505 |

---

## 3.2 Experimental Results

Figure 2 shows the measured profile of the incident beam just in front of the stack of plates.

The doses in this and all following results are normalized to an incident flux of $5 \times 10^9$ equivalent quanta. The flux measured in the center of the beam is due mainly to cascade formation in the air path, while the wings are due to back scattering from the material. This is noticeably stronger in the case of lead, as was shown again by measurements in the stack. In the case of copper and concrete, omission of the plates behind the ionization chamber

produced no measureable difference in comparison with the measurements with further plates behind it. Figures 3a - 3c show the integral over the lateral distribution plotted against the penetration depth t of the cascade. The ordinate gives the percentage of incident energy lost in each plate of thickness $X_o$ (1 radiation length). In the integration, the last used interval contributed only 0.5% to the final value.

Longitudinal development of the electromagnetic cascade in heavy concrete, copper, and lead; measured values and Monte-Carlo calculations are shown. The ordinate gives the percentage of incident energy absorbed in one plate of thickness $X_o$. For concrete, a curve is drawn in through the experimental points. The last point of the lead curve is too low because of the lack of further back scattering.

The transition curves obtained for copper and lead can be compared with Monte-Carlo calculations due to Völkel[11]. These calculations allow for, in the case of electrons, bremsstrahlung, Moller scattering, multiple scattering, and ionization losses, and in the case of photons for pair production, Compton scattering and photoelectric

effects. Electrons were followed down to a cutoff energy of 1.5 Mev; photons to 0.25 Mev. In the case of copper, (Figure 3b), the rate of energy loss was calculated both for incident 6 Gev electrons, and also for an incident bremsstrahlung spectrum having a maximum energy of 6 Gev. As can be seen, these calculated curves differ only at the beginning of the cascade. The calculated curve for an incident bremsstrahlung spectrum agrees very well with the experimental values. In the case of lead, calculations are only available for incident electrons, so that the experimental and the theoretical curves differ slightly at the start of the cascade (Figure 3c).

The position of the maximum can be expressed by the formula:

$$t_{max} = \ln(E_o/E_c) - k \qquad (1)$$

where $t_{max}$ is measured in radiation lengths, $E_o$ is the initial energy, and $E_c = E_{crit}/2.3$. Ott[15] gives values of $k$ as 1.3 for lead and 1.6 for copper, both values agreeing well with the experimental results.

The decay of the cascade is approximately exponential with the minimum absorption coefficient for the particular material.

Table 1 shows the coefficients deduced from Figure 3 ($\lambda_{cascade}$) together with the minimum absorption coefficient ($\lambda_{min}$). Within the limits of experimental error, these values agree for copper and lead, but the cascade in heavy concrete decays more slowly than would be given by the minimum absorption coefficient. This difference can probably be traced back to the wide absorption minimum of materials with low Z, in which photons suffer little deviation from the forward direction as a result of Compton scattering.

The doses measured on the axis of the cascade are plotted against the cascade length in cm in Figure 4. They give the maximum dose measured behind a shield of given thickness, as a result of an incident beam of $5 \times 10^9$ equivalent quanta at 6.3 Gev. The curve for lead ($\lambda(0^o)$ in Table 1) falls off far more rapidly than expected from the minimum absorption coefficient, because the low-energy particles are scattered away from the axis. In the case of copper and concrete, the curve falls as predicted by the minimum absorption coefficient, i.e. for the reasons given above, more rapidly than the curves in Figure 3.

Figure 5 shows the general distribution of radiation measured behind concrete, both parallel and perpendicular to the cascade axis. Lines of equal dose rate are drawn in.

## 4. Production of neutrons by the electromagnetic cascade

As mentioned in the introduction, the production of particles due to cascades produced by incident 6.3 Gev bremsstrahlung was examined, in addition to the development of the cascade itself. The photoproduction of neutrons and protons at complex nuclei is due to three main processes. At low Y-ray energies (10-20 Mev) photons are absorbed mainly through resonance as a result of a dipole interaction (giant resonance). Decay of the compound nucleus thus formed generally gives a (Y,n) or a (Y,p) reaction. The collision cross-sections for these are known. Processes like (Y,2n), (Y,np), and so on are less frequent.

At higher energies, the collision cross-sections for this type of photon absorption fall rapidly because the shorter wavelength of the photon prevents interaction with the entire nucleus, and

interaction proceeds only with part of the nucleus. Mainly n-p pairs are produced by photo-splitting of quasi-deuterons. According to Levinger[18], above energies of about 100 Mev the collision cross-section for this type of reaction can be written :

$$\sigma(\gamma,np) = L(NZ/A)\sigma_D \qquad (2)$$

where N and Z are the numbers of neutrons and protons respectively, and A is the atomic weight of the nucleus. $\sigma_D$ is the known collision cross-section for the photo-splitting of deuterons. Levinger gives the value of L as 6.4, but measurements to determine this quantity give contradictory results (see section 4.2.2).

Above energies of 300 Mev, the cross-section for this reaction falls off approximately as the third power of the photon energy, so that above 500 Mev this reaction is no longer of importance. Particle production in this high-energy region is the result of photon-production of $\pi$-mesons. Using nuclear tracking plates, Roos and Peterson[19] showed that in complex nuclei about 80% of the $\pi$-mesons produced are absorbed in the same nucleus. Generally, this leads to the development of an intranuclear cascade, followed by a damping

process and then to 'star' production, so that the net result is the emission of low-energy neutrons and protons.

Since knowledge of the collision cross-sections is sufficient in the reactions listed above, except in the region of main resonance, calculations of particle production in thick targets where the electromagnetic cascade is fully developed become increasingly inaccurate. To obtain experimental information on this point for the case of incident 6 Gev bremsstrahlung, we examined the production of low-energy neutrons in two bands (1 kev to 10 Mev and 2.5 Mev to 25 Mev) and of high-energy neutrons and protons above 25 Mev. Cylindrical targets of aluminum, copper, and lead were used. In addition, the spreading out of neutrons of energy below 25 Mev was studied in stacks of plates of copper and lead placed in the same way as in section 3.

## 4.1 Neutrons with energy below 25 Mev

### 4.1.1 M e t h o d

The flux density of low-energy neutrons below 10 Mev can easily be measured with the aid of an activation method[20,21]. An

indium foil (2.9 cm in diameter, thickness 0.01 cm) is placed in the center of a paraffin wax sphere (15 cm in diameter) covered with a layer of cadmium. The β-activity of the foil due to the (n,γ) reaction with 'thermalized' neutrons is measured. The sensitivity curve of this arrangement was determined with the van der Graf accelerator of the IInd Physical Institute of the University of Hamburg, using the common neutron-producing reactions $t(p,n)He^3$ and $t(d,n)He^4$. The results are shown in Figure 6, together with curves from refs. 20 and 21. It is assumed that this method is sensitive to neutrons between 1 kev and 10 Mev. The smallest measurable neutron flux is about 0.5 $n/cm^2 sec$.

In the measurements on the stacks of plates the sphere is directly in a high-energy beam, and one has to be sure that no unwanted β-activity can occur. The time decay of the indium activity was measured over a period of 10 half-lives and no variation from the standard 54 min half-life was found. Only after that length of time was a long half-life component discovered, probably due to the reaction $In^{115}(\gamma,n)In^{114}$ with a half-life of 49 days. It was also

shown that if the paraffin wax was removed from the cadmium shell, the activity of the indium was only 2 to 3% of that with the paraffin wax present, all other conditions being equal. Thus the activity is due to epithermal neutrons, and the spurious activity produced by high-energy neutrons or Y-rays need not be considered.

Since low-energy neutrons were measured by the indium-paraffin wax sphere, the background level in the concrete-walled experimental region was high. Measurements on the thick targets were made at various distances, to determine the necessary correction factors.

The upper limit of 10 Mev of the indium-paraffin wax method is rather low for the study of the giant resonance neutrons, and for this reason activation measurements of the (n,p) reaction on phosphorus were carried out. The cross-section for this reaction is shown in Figure 7, and a mean value of 82 mb was used in the calculations. We assume that this reaction measures neutrons in the energy range of 2.5 to 25 Mev.

The use of this reaction, whose cross-section is 3 orders

of magnitude smaller than the $(n,\gamma)$ reaction on indium described above, leads to difficulties if, when placed in a high-energy beam, a large number of side reactions are energetically possible as well as the one required for the detection of neutrons. However, all nuclei lighter than $P^{31}$ have half-lives one magnitude longer or shorter than that of $Si^{31}$, with the exception of $F^{18}$. The cross-section for the production of $F^{18}$ from $P^{31}$ by high-energy neutrons or protons is not known, but it can be estimated at $\sim 5$ mb from the production of $F^{18}$ from other nuclei (see for example the synthesis due to Bruninx[22]). The cross-section for the photoproduction of $F^{18}$ from $P^{31}$ is about 0.5 mb (from estimates similar to the considerations mentioned in section 5). In fact, no deviation from the known half-life of $Si^{31}$ occurred before 5 half-life periods during measurements made on the copper plate stack; only after this time was an unidentified longer-lived reaction product observed. The competing reaction, $P^{31}(p, p\tilde{\pi}^{+})Si^{31}$ can be neglected.

For the measurement, 4 g of powdered red phosphorus were

sealed into a small polythene bag. After irradiation, the phosphorus was shaken onto flat dishes and its β-activity was determined with a $2\pi$ -flux counter provided with an anti-coincidence device. The neutron sensitivity of the method was found by calibration against a Po-Be source, allowing for the change of cross-section with the known neutron-spectrum of the source. With a zero reading of the β-counter of 0.1 pulses per minute and a useful counter area of 1 $cm^2$, the smallest measurable neutron flux was about 100 $n/cm^2 sec$.

Background measurements in the experimental region show that the background radiation is not important in measurements on phosphorus.

The experimental errors in these activation measurements are about 15 to 20%.

### 4.1.2 Experimental Results and Discussion

a) Measurements on thick targets

To find the number of neutrons produced with energies below 25 Mev, largely the giant-resonance neutrons, a target having an

optimum size must be used, i.e. one that is sufficiently thick to allow maximum neutron production by low-energy photons, and yet not so large that the neutrons are absorbed to an appreciable extent. Neutron multiplication by the (n,2n) reactions, or 'star' formation need not be considered. The length of target necessary for this optimum condition was studied, in the case of lead, with the indium-paraffin wax sphere. After 10 cm of lead the neutron production rate became constant, while 50 and 90% of this rate were observed through 4 cm and 7 cm respectively. These values agree with the above-mentioned Völkel's Monte-Carlo calculations[11], which show that for an incident beam of 6 Gev electrons or Y-rays the maximum number of photons with energies in the range of 10 to 20 Mev occurs around 7 radiation lengths, equivalent to 4 cm. Various measurements were made on copper to find the diameter of the optimum target. A change of diameter from 5 cm to 12 cm increased the neutron production rate by only 10 to 20%, which is understandable considering the small lateral spread of the electromagnetic cascade. The length of the optimum target for copper was 25 cm. The aluminum target was 110 cm long, with a diameter of 20 cm.

The angular distribution of the low-energy neutrons was examined with both detecting methods using a 10 cm long copper target. Within the limits of experimental error, the indium-paraffin wax sphere showed an isotropic distribution; the phosphorus method showed a small forward maximum, with 60% of all neutrons between 0 and $90^{o}$. Giant resonance neutrons thus have an angular distribution symmetric over $90^{o}$, or possibly even isotropic, whether they are produced by evaporation of a compound nucleus or are emitted by a direct interaction[18]. A fraction of neutrons with energies around 10 Mev is then due to high-energy processes.

The results of integration over the angular distribution of the neutrons produced, and normalised to an incident flux of $5.10^{9}$ equivalent quanta are shown in lines 1 and 2 of Table 3. Since the energy ranges of the two detecting methods partly overlap, the total number of neutrons below 25 Mev was arbitrarily taken as the number detected by the indium-paraffin wax method, plus half those measured with the phosphorus. These numbers are shown in line 3. The total experimental error is then about 25%.

The measured values can now be compared with general estimates to test the usefulness of this easily performed calculation. Let $\sigma(k)$ be the reaction cross-section of a process in which a particle is produced from a $\gamma$ quantum with an energy $k$ above the threshold energy for the process, $E_s$.

If the target is sufficiently thick for the electromagnetic cascade produced by an electron or photon of energy $E_o$ to be fully developed, then the track length, and thus the distance traveled by all cascade photons with energies between $k$ and $k + dk$ is given approximately by

$$g(E_o,k)dk = 0.57\ X_o(E_o/k^2)dk \qquad (3)$$

(see Rossi[13]). $X_o$ is the radiation length of the target material. Only pair production and bremsstrahlung in the cascade are allowed for in the derivation of this equation. Zerby and Moran[23] have shown by Monte-Carlo calculations which included Compton effect and ionization losses, that eq. (3) is a good approximation for $\gamma$ energies $k$ in the range

$$E_c < k < 0.6\ E_o \qquad (4)$$

(where $E_c$ is the critical energy).

The particle yield per incident electron or equivalent Y quantum comes out as :

$$Q = n \int_{E_s}^{E_o} \sigma(k) g(E_o, k) dk \qquad (5)$$

n being the number of atoms per $cm^3$.

Ref. 24 gives the integrated cross-section up to 25 Mev together with the corresponding resonance energies necessary for the calculation of the yield of giant resonance neutrons. The results of these calculations are shown in line 4 of Table 3. Y-Quanta with energies in excess of 25 Mev also contribute to the production of low-energy neutrons, this contribution can be estimated from a paper by Jones and Terwilliger[25]. The latter authors determined the production cross-section for neutrons by Y-rays with energies up to 320 Mev, using a long counter as a neutron detector. It is known that the sensitivity of this device falls sharply above 14 Mev, so that we can assume any detected neutrons to have energies below 25 Mev. This means that we can use the neutron cross-sections measured by Jones and Terwilliger in the calculations of the neutron yield. The

total number of neutrons with energies below 25 Mev produced by Y-quanta up to 320 Mev is shown in line 5 of Table 3.

Table 3. Numbers of neutrons or protons in various energy ranges produced by 6.3 Gev bremsstrahlung in optimum targets made of aluminum, copper or lead. Incident beam normalised to $5.10^9$ equivalent quanta

| | Al | Cu | Pb |
|---|---|---|---|
| 1) No. of neutrons between 1 kev and 10 Mev (measurement) | $4.4 \times 10^9$ | $9.6 \times 10^9$ | $10.8 \times 10^9$ |
| 2) No. of neutrons between 2.5 Mev and 25 Mev (measurement) | 2.3 | 2.6 | 4.5 |
| 3) No. of neutrons below 25 Mev =(row 1) + 0.5 (row 2) | 5.6 | 10.9 | 13.0 |
| 4) No. of low-energy neutrons produced by Y-quanta with energies below 25 Mev (estimate) | 3.8 | 7.0 | 10.4 |
| 5) No. of low-energy neutrons (below 25 Mev) produced by Y-quanta with energies below 320 Mev (estimate) | 6.0 | 9.2 | 12.0 |
| 6) No. of neutrons and protons with energies above 25 Mev (measurement) | $0.88 \times 10^9$ | $0.60 \times 10^9$ | $0.42 \times 10^9$ |
| 7) No. of protons and neutrons produced by the splitting of quasi-deuterons (estimate) | 0.29 | 0.16 | 0.080 |
| 8) No. of neutrons and protons with energies above 25 Mev produced by meson reactions (estimate) | 0.06 | 0.03 | 0.02 |

As can be seen, there is a good agreement between the experimental results and the simplified estimates made using equations (3) and (5), even though, in the case of aluminum, eq.(4) no longer holds for the giant resonance neutrons. Apparently the measurement range of the indium-paraffin wax sphere is adequate to detect the giant resonance neutrons, whereas the total number of neutrons with energies below 25 Mev, a considerable fraction of which are due to high-energy processes, is best measured by the combination of the indium-paraffin wax sphere with a phosphorus detector.

The production rate for giant resonance neutrons was also measured when the incident beam of bremsstrahlung had a maximum energy of 3.0 Gev. As expected, this showed (within an experimental error of 10%) that in this energy range, the yield of neutrons is proportional to the maximum bremsstrahlung energy.

b) Measurements on plate stacks

The distribution of low-energy neutrons was studied by both detecting methods in the copper and lead stacks described in

section 3. Since the paraffin sphere had a diameter of 15 cm, only one was introduced into the stacks, whereas the several phosphorus samples were irradiated in different gaps at the same time. Figures 8 and 9 show the neutron flux densities obtained in this way, measured in the direction of the beam, normalised for an incident beam of $5 \times 10^9$ equivalent quanta per second. The measured maxima of these curves again coincide with the maximum number of $\gamma$-rays in the cascade with energies between 10 and 20 Mev (compare subsection a).

The relation governing the curve maximum for a material does not agree with the production rates as measured by the two methods. This is because the two methods measure an average flux density over the volume of the detector, and this is very different in the two cases.

In order to give a number to the decay of neutron flux as measured by the phosphorus detector, it is necessary to assume an equation of the form :

$$\phi \approx (1/r)e^{-\Sigma r} \qquad (6)$$

taken from diffusion theory. By fitting this to the results, we

obtain values of the macroscopic reaction cross-section $\Sigma$, being 0.18 $cm^{-1}$ for copper (for distances between 10 and 50 cm from the maximum) and 0.29 $cm^{-1}$ for lead (distances 6 to 22 cm from the maximum). The phosphorus method has a lower detection limit of 2.5 Mev, which corresponds to the condition for the measurement of removal-reaction cross-sections in reactor shielding. However, the results for lead are noticeably different from the usual values of the removal-reaction cross-section, (0.12 $cm^{-1}$ for lead, 0.21 $cm^{-1}$ for copper) because of the different neutron spectrum. The value of $\Sigma$ is higher in lead than in copper because fewer high-energy neutrons are produced in lead (see section 4.2 and line 6 of Table 3).

The rate of fall of the neutron component measured by the indium-paraffin wax sphere is considerably slower, because the decay in the number of high-energy neutrons is superimposed on the build-up of low-energy neutrons. Obviously, equilibrium between high-energy (10 Mev) and low-energy ( $< 1$ Mev) neutrons has not yet set in, even at the largest distances measured. Moreover, at small distances, the size of the detector has an effect on the rate of fall of the curves.

That a pure exponential function is obtained (within the experimental error), is probably due to chance. The decay coefficients taken from the gradient of the straight part, which therefore allows for the dependance on distance, are 0.11 $cm^{-1}$ for copper and 0.095 $cm^{-1}$ for lead.

## 4.2 Neutrons with energies above 25 Mev

### 4.2.1 M e t h o d

A well known activation method for the detection of high-energy neutrons and protons is the activation of plastic scintillators by the reaction $C^{12}(n,2n)C^{11}$. The reaction threshold is 20 Mev. However, with electron accelerators this reaction can only be used in special cases since it is generally masked by the $(\gamma,n)$ process. A choice of an alternative reaction must allow for the desirability of a high $\gamma$-threshold, whilst keeping the neutron threshold around 20 Mev. If chemical separation is to be avoided, only reactions on light nuclei can be considered, as otherwise the number of competing reactions becomes too large.

The reactions used for the detection of high-energy

neutrons and protons were $Na^{23}(n, 2p4n)F^{18}$ and $Na^{23}(p, 3p3n)F^{18}$ $F^{18}$ is a β-emitter, with a half-life of 1.8 hours. The reaction cross-section for protons is known with sufficient accuracy[22,26,27] (see Figure 10). Only one value, at 90 Mev[28], is known for neutrons, but the cross-section should not differ significantly from that for protons, when measured from the threshold energy. A mean value of 15 mb was assumed for the calculations. The probes were made of 4 g of $Na_2O_2$ sealed in plastic bags. The smallest detectable neutron flux density was about 7000 $n/cm^{-2}sec^{-1}$.

In preliminary experiments, we discovered that the β-emitters $C^{11}$ and $N^{13}$ formed in the sample no longer disturb the measurements about an hour after the end of activation. The formation of $Na^{22}$ can be neglected because of its half-life of 2.6 years. The formation of $Na^{24}$ (with a half life of 15.4 hours) could not be prevented, despite cadmium shielding around the sample. Separation of the activities of $F^{18}$ and $Na^{24}$ therefore required two measurements of β-activity. The optimum separation of these two

measurements was found to be between 5 and 15 hours. The reaction $O^{18}(p,n)F^{18}$ is of no importance owing to the rarity of $O^{18}$ (0.2%).

Since the chosen detection method cannot be calibrated, the β-activity of the $Na_2O_2$ sample has to be determined absolutely. The calculation of the self-absorption of β-rays in $Na_2O_2$ required in the determination was performed by the method due to Dalton and Kunaish[29]. The function $E_3(\mu\tau)$ used by them has been tabulated by Beckurts and Wirtz[30]. As a check, these self-absorption calculations were applied to the $P^{31}(n,p)Si^{31}$ and $In^{115}(n,\gamma)In^{116}$ reactions using a calibrated neutron source. Good agreement between experimental and calculated self-absorptions was obtained for phosphorus and indium.

### 4.2.2 Results and Discussion

The angular distribution of neutrons and protons with energies above 25 Mev was measured on a 10 cm long copper target (Figure 11). The sharp maximum below $30^{\circ}$ is due to high-energy γ-rays (see section 5). The angular distribution of electrons and γ-radiation was measured with a small ionization chamber, and shows

that above $30^{\circ}$ only neutrons were detected. The curve was therefore extrapolated to between 0 and $30^{\circ}$. As can be seen, forward scattering is strongly preferred in the energy range above 25 Mev, some 70% of all particles leaving the target with scattering angles smaller than $90^{\circ}$.

The total number of neutrons and protons above 25 Mev produced by the various targets is shown in line 6 of Table 3, the incident flux being normalized to $5 \times 10^{9}$ equivalent quanta.

These values will again be compared with estimates. The two production reactions that must be considered are stated at the beginning of section 4.2. The reaction cross-section for the production of high-energy neutrons and protons by the splitting of quasi-deuterons in the nucleus is given by eq. (2). The cross-section for photosplitting of deuterons, $\sigma_D$, is known[38-40] and can be approximated by :

$$\begin{aligned} \sigma_D &= \frac{7 \times 10^3}{k} \ \mu b && \text{for} \quad 50 \text{ Mev} < k < 125 \text{ Mev} \\ &= 57 \ \mu b && \text{for} \quad 125 \text{ Mev} < k < 300 \text{ Mev} \\ &= \frac{1.3 \times 10^9}{k^3} \ \mu b && \text{for} \quad 300 \text{ Mev} < k \end{aligned} \qquad (7)$$

Experimentally determined values of the constant L are at variance. They rely on measurements of neutrons and protons ejected in coincidence[31,32], measurements on radioactive end-products[33], and measurements of all the neutrons and protons with energies above 25 Mev leaving a carbon target[34]. Allowances must be made, for example, for the fact that one of the two nucleons may be scattered in the producing nucleus, and be consequently lost to a coincidence measurement, or that in the splitting of the quasi-deuteron reaction further nucleons are emitted in an evaporation process, so that a different final nucleus is formed. After allowing for such effects, a value of $L = 3$ was chosen. Protons with energies above 200 Mev can pass through 10 cm of aluminum or 5 cm of copper or lead, and this was allowed for by introducing a factor of 2 when $\gamma$ energies above 300 Mev were used in (7). Using equations (7), (5) and (3), the numbers of neutrons and protons produced were obtained; these are listed in line 7 of Table 3.

Estimates of the production of high-energy neutrons and protons by meson effects were made with the aid of a paper by Roos

and Peterson[19]. If we assume that results obtained with nuclear emulsion plates for nuclei of mean atomic weight of 50 can be extrapolated to other nuclei, we obtain the following data :

a) The reaction cross-section for the production of stars with 2 or more arms is about 250 μb per nucleon for γ-energies above 250 Mev. This number must be multiplied by the atomic weight A for a nucleus.

b) The mean number of arms per star is approximately

$$\bar{p} = 0.14\sqrt{k} \quad \text{for} \quad k > 250 \text{ Mev} \tag{8}$$

c) For γ-rays with k = 1150 Mev, most of the arms of a star were identified as proton tracks, with around 10% having an energy greater than 25 Mev. According to the Monte-Carlo calculations of Dostrovsky et al.[35], the number of neutrons emitted in an evaporation process approximates to the number of charged particles. We therefore assume that the number deduced in b) must be multiplied by 0.1 to obtain the number of neutrons emitted with energies greater than 25 Mev. The protons need not be considered, as their energy is too low.

d) As mentioned at the beginning of section 4, around 80% of all

interactions between high-energy photons and complex nuclei lead to star production (see (a) to (c) ). In roughly 20% of all cases the $\pi$-mesons produced leave the nucleus without interaction. Since they can produce further nuclear reactions, this fraction will be fully considered.

With this data, we obtain a fairly good value for the cross section for the production of neutrons and protons with energies above 25 Mev, through high-energy quanta of energy k:

$$\sigma = 3.5 \times 10^{-30} A \sqrt{k} + 5 \times 10^{-29} A \quad \text{for} \quad k > 250 \text{ Mev} \tag{9}$$

The yield, which can now be calculated from equations (9), (5), and (3), is given in line 8 of Table 3.

The table shows to what extent the various processes contribute to neutron production. It also shows that the two estimates in lines 7 and 8 cannot explain the number of neutrons and protons measured by the $Na_2O_2$ sample. Recent measurements of neutron production rates by $\gamma$ rays up to 200 Mev[43] give the unusually high value of 10 to the constant L in equation (2). This would explain our results from the splitting of quasideuterons in the case of

copper and aluminum, but calculations on the lead target still give a value which is 60% too low. This discrepancy is probably due to the much larger number of low-energy neutrons (lines 3 and 5). If only a fraction of these neutrons had energies above 25 Mev, the experimental results given in line 6 could be explained. This would imply that most of the neutrons detected by the $Na_2O_2$ method had relatively low energies, possibly lying between 25 and 100 Mev.

## 5. Other measurements

At first it was planned to study the distribution of neutrons above 25 Mev in the copper stack, using the $Na_2O_2$ sample. However, measurements in the beam direction gave a maximum, followed by a steeply falling exponential ($\lambda = 0.35$ cm$^{-1}$), and the cross-sectional distribution gave a very small conical spread, with a cone semi-apical angle of only $5^{\circ}$. This shows that the $Na_2O_2$ sample was activated by high-energy photons rather than by neutrons. In fact, Monte Carlo calculations by Völkel show that, with incident 6 Gev electrons, photons in the energy range of 400 to 1000 Mev have a decay coefficient between 0.3 and 0.4 cm$^{-1}$ in copper. The calculated and experimentally obtained positions of the maximum are also

in agreement. We then attempted to calculate quantitatively, with the aid of the papers by Roos and Peterson and by Völkel, the photon-induced activation of an $Na_2O_2$ sample in the copper stack. We assumed that the results from nuclear emulsion plates applied to the sodium nucleus. The transmutation of $Na^{23}$ into $F^{18}$ requires the emission of 2 protons and 3 neutrons. According to Roos and Peterson, the probability that a photostar has two arms is about 0.4. The probability of the emission of 2 protons and 3 neutrons is then about 0.3. From this it follows that the required cross-section for the transmutation of $Na^{23}$ to $F^{18}$ by high-energy photons is 250 x 23 x 0.3 μb = 1.7 mb. The flux density of photons above 300 Mev can be obtained from Monte-Carlo calculations and the known beam diameter. The $F^{18}$ activity of the $Na_2O_2$ sample is then easily calculated, and we obtained good agreement with the experimental values. It seemed to us quite interesting that with the use of the papers mentioned the yield of a relatively complex photon reaction could be fairly accurately predicted.

We also tried to measure the neutrons and protons above 700 Mev in the stacks, using the production of $Tb^{149}$ from $Au^{197}$ (see refs. 36 and 37). The intensity of our bremsstrahlung was just sufficient to determine the α-activity of $Tb^{149}$. Here again, however, we discovered from the value of the decay coefficient that photoproduction of $Tb^{149}$ in the gold film masked the desired process. It seems to be difficult to detect high-energy neutrons in the presence of high-energy photons by activation methods.

R e f e r e n c e s


1) W. Blocker, R.W. Kenney und W.K.H. Panofsky, Phys.Rev. 79 (1950) 419

2) A. Kantz und R. Hofstadter, Phys.Rev. 89 (1953) 607

3) Y. Murata, J.Phys.Soc. Japan 20 (1965) 209

4) J.W. Cronin, E. Engles, M. Pyka und R. Roth, Rev.Sci.Instr. 33 (1962) 946

R. Kajikawa, J.Phys.Soc. Japan 18 (1963) 1365

B. Agrinier, Y. Koechlin, B. Parlier, G. Boella, G. Degli Antoni, C. Dilworth, L. Scarsi und G. Sironi, N.Cimento 36 (1965) 1077

5) M.D. Wilson und I.B. McDiarmid, Can.J.Phys. 40 (1962) 573

6) S. Lal und A. Subramanian, Nuovo Cim. 26 (1962) 1245

7) E.E. Becklin und J.A. Earl, Phys.Rev. 136 (1964) B 237

H. Thom, Phys.Rev. 136 (1964) B 447

8) C.A. Heusch und Ch.Y. Prescott, Phys.Rev. 135 (1964) B 772

9) H. Lengeler, W. Tejessy und M. Deutschmann, Z.Physik 175 (1963) 283

10) W.R. Nelson, Th.M. Jenkins, R.C. McCall und J.K. Cobb, Stanford Linear Accelerator Center, SLAC-PUB-163 (1966)

11) U. Völkel, Deutsches Elektronen-Synchrotron, DESY 65/6 (1965) und private Mitteilung

12) M.S. Livingston und J.P. Blewett, Particle Accelerators (McGraw-Hill Book Company, 1962)

13) B. Rossi und K. Greisen, Rev.mod.Phys. 13 (1941) 240

B. Rossi, High-Energy Particles, Prentice-Hall, Inc., Englewood Cliffs, N.Y. (1956)

14) O.I. Dovzhenko und A.A. Pomanskii, Sov.Phys.JETP 18 (1964) 187

15) K. Ott in Kosmische Strahlung (Hrsg. W. Heisenberg), Springer-Verlag,Berlin, Göttingen, Heidelberg (1953)

16) K. Pinkau, Phys.Rev. 139 (1965) B 1548

17) F.W. Spiers, Radiation Dosimetry (Hrsg. G.J. Hine und G.L. Brownell), Academic Press, New York (1956)


---

11) U. Völkel, German Electron Synchrotron, DESY Report 65/6 (1965) and private communication.

15) K. Ott in 'Cosmic Radiation' (ed. by W.Heisenberg) Springer-Verlag, Berlin, Göttingen, Heidelberg (1953).

18) J.S. Levinger, Phys.Rev. 84 (1951) 43
J.S. Levinger, Nuclear Photo-Disintegration, Oxford University Press (1960)

19) C.E. Roos und V.Z. Peterson, Phys.Rev. 124 (1961) 1610

20) R.G. Wallace, B.J. Moyer, H.W. Patterson, A.R. Smith und L.D. Stephens, in Selected Topics in Radiation Dosimetry, IAEA Wien (1961)

21) L.D. Stephens und H. Aceto, in Neutron Dosimetry, Vol. I IAEA Wien (1963)

22) E. Bruninx, CERN, CERN-Bericht 61-1(1961) und 64-17(1964)

23) C.D. Zerby und H.S. Moran, J.Appl.Phys. 34 (1963) 2445

24) Shielding for high-energy electron accelerator installations, National Bureau of Standards Handbook 97 (1964)

25) L.W. Jones und K.M. Terwilliger, Phys.Rev. 91 (1953) 699

26) P.A. Benioff, Phys.Rev. 119 (1960) 316

27) J.W. Meadows und R.B. Holt, Phys.Rev. 83 (1959) 47

28) W.J. Knox, Phys.Rev. 75 (1949) 537

29) G.R. Dalton und H.H. Kunaish, Intern.J.Appl.Rad.Isot. 15 (1964) 301

30) K.H. Beckurts und K. Wirtz, Neutron Physics, Springer-Verlag Berlin, Göttingen, Heidelberg (1964)

31) P.C. Stein, A.C. Odian, A. Wattenberg und R. Weinstein, Phys.Rev. 119 (1960) 348

32) J. Garvey, B.H. Patrick, J.G. Rutherglen und I.L. Smith, Nucl. Phys. 70 (1965) 241

33) J.R. Van Hise, R.A. Meyer und J.P. Hummel, Phys.Rev. 139 (1965) B 554

34) P.S. Baranov, V.J. Gol'danskii und V.S. Roganov, Phys.Rev. 109 (1958) 1801

35) I. Dostrovsky, P. Rabinowitz und R. Bivins, Phys.Rev. 111 (1958) 1659

36) E. Bruninx, Nucl.Phys. 64 (1965) 481

37) E.M. Franz und G. Friedlander, Nucl.Phys. 76 (1966) 123

38) L. Allen, Phys.Rev. 98 (1955) 705

39) J.C. Keck und A.V. Tollestrup, Phys.Rev. 101 (1956) 360

40) H. Meyers, R. Gomez, D. Guinier und A.V. Tollestrup, Phys.Rev. 121 (1961) 630

41) P. Cuzzocrea, G. Pappalardo und R. Ricamo, N. Cimento 16 (1960) 450

J. Kantele und D.G. Gardner, Nucl.Phys. 35 (1962) 353

42) R.E. Bullock und R.G. Moore, Phys.Rev. 119 (1966) 721

43) G. Bishop, S. Costa, S. Ferroni, R. Malvano und G. Ricco, N. Cimento 42 B (1966) 158

oooooooooooooooooooooooo

Figure 1. Experimental layout. The plate stacks and the thick targets were placed at the point marked 'target'.

Figure 2. The profile of the incident beam in front of the stack of plates measured with the small ionization chamber (30 $mm^3$). The difference between the back scattering of lead and concrete is noticeable.

Figure 3a-3c Longitudinal development of the electromagnetic cascade in heavy concrete, copper, and lead; measured values and Monte-Carlo calculations are shown. The ordinate gives the percentage of incident energy absorbed in one plate of thickness $X_o$. For concrete, a curve is drawn in through the experimental points. The last point of the lead curve is too low because of the lack of further back scattering.

Figure 4. The dose on the axis of the cascade as a result of an incident beam of $5 \times 10^9$ equivalent quanta plotted against the thickness of material.

Figure 5. Curves of equal dose in heavy concrete for an incident rate of $5 \times 10^9$ eq. quanta. The doses are measured in rads.

Figure 6. Sensitivity curve of indium-paraffin wax sphere. The ordinate gives the count rate in a $2\pi$ counter at a neutron flux of 1 $cm^2 sec^{-1}$ and saturated activation.

Figure 7. The collision cross-section of the $P^{31}(n,p)Si^{31}$ reaction. (see ref. 41 and also refs. 42 and 28).

Figure 8. Neutron flux density in copper, measured in the beam direction, for an incident flux of $5 \times 10^9$ eq. quanta.

Figure 9. Neutron flux density in lead, measured in the beam direction, for an incident flux of $5 \times 10^9$ eq. quanta.

Figure 10. Reaction cross-sections for $Na^{23}(p,3p3n)F^{18}$ and $Na^{23}(n,2p4n)F^{18}$.

Figure 11. Angular distribution of neutrons and protons with energies above 25 Mev (solid curve), measured with a copper target.

Abb.1

Figure 1

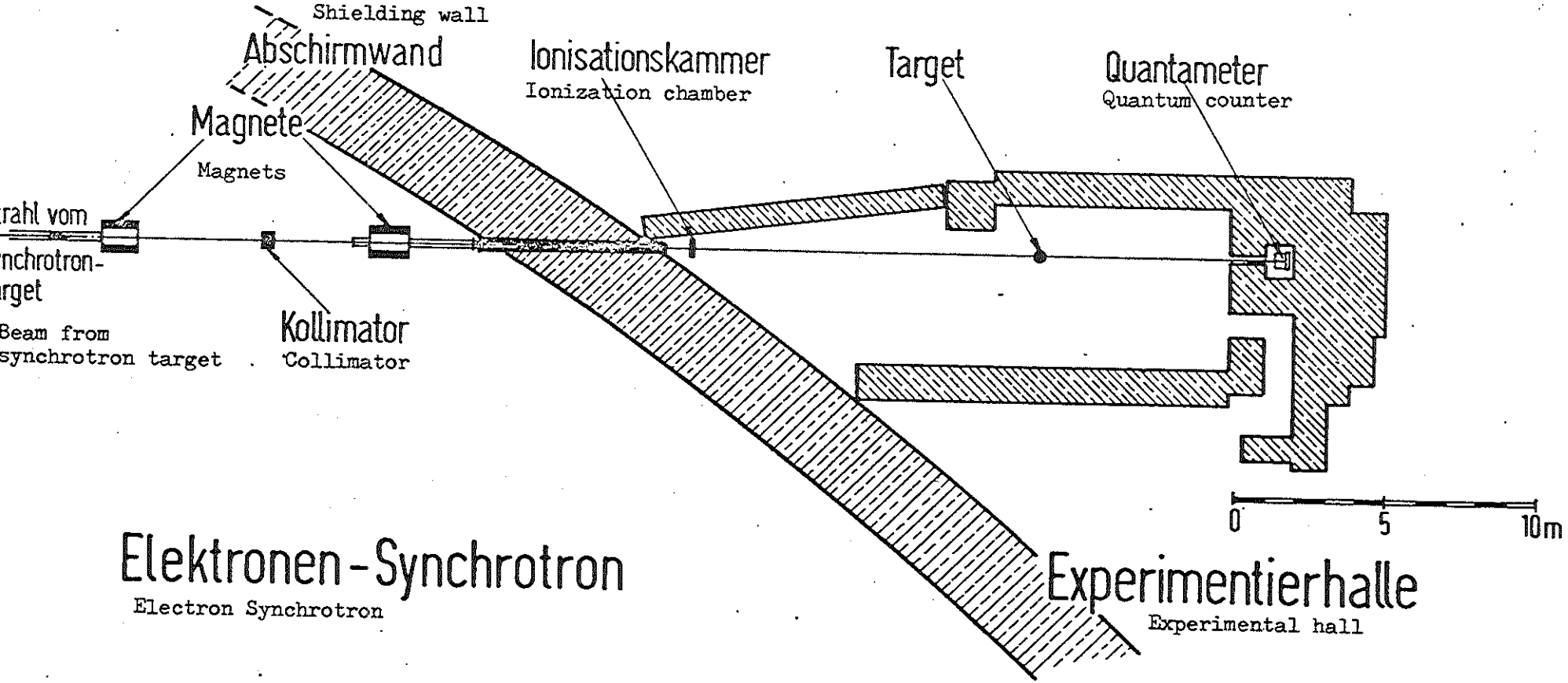

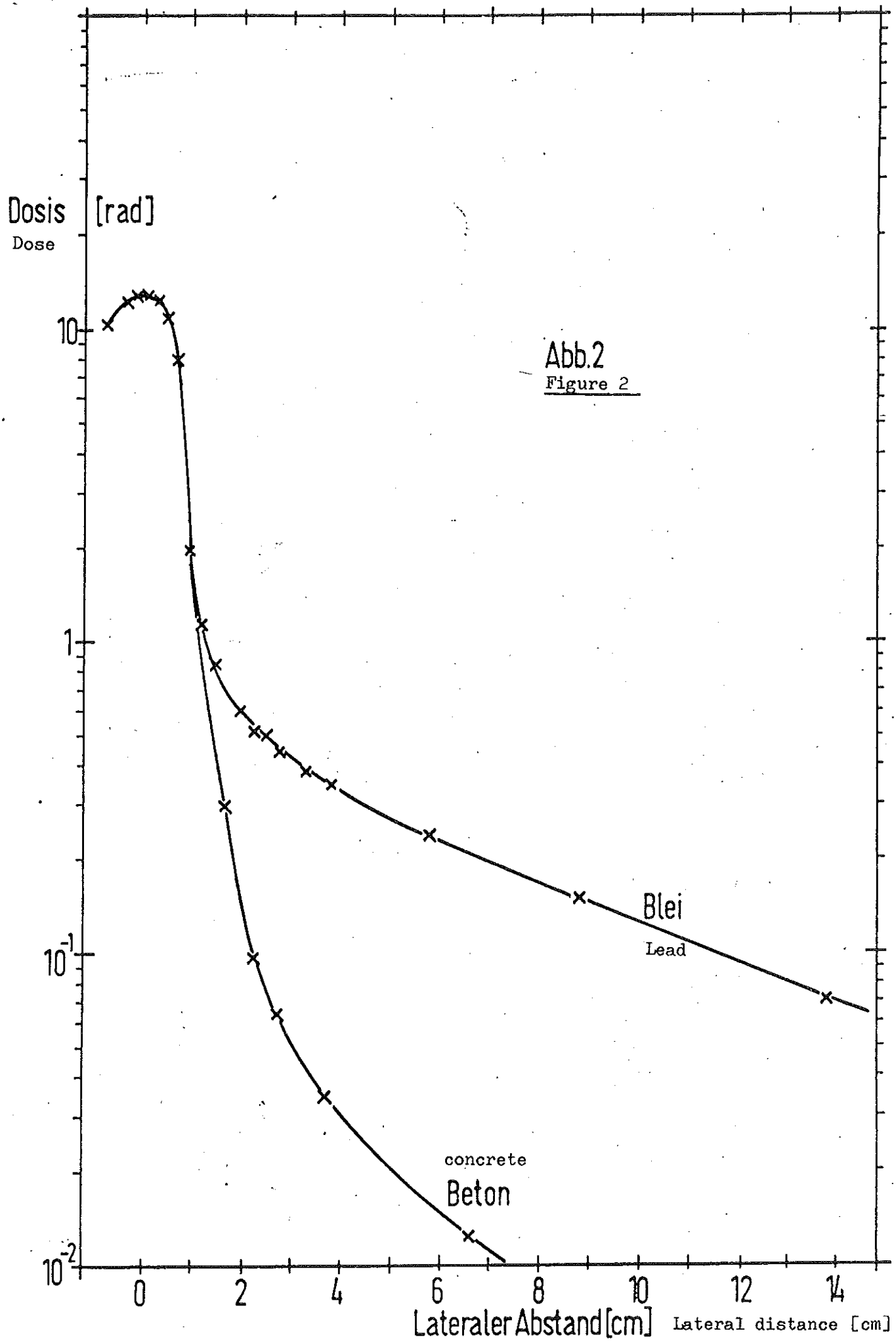


Abb.2
Figure 2

Figure 3a. Heavy concrete

Abb. 3a – Schwerbeton

Meßwerte experimental points

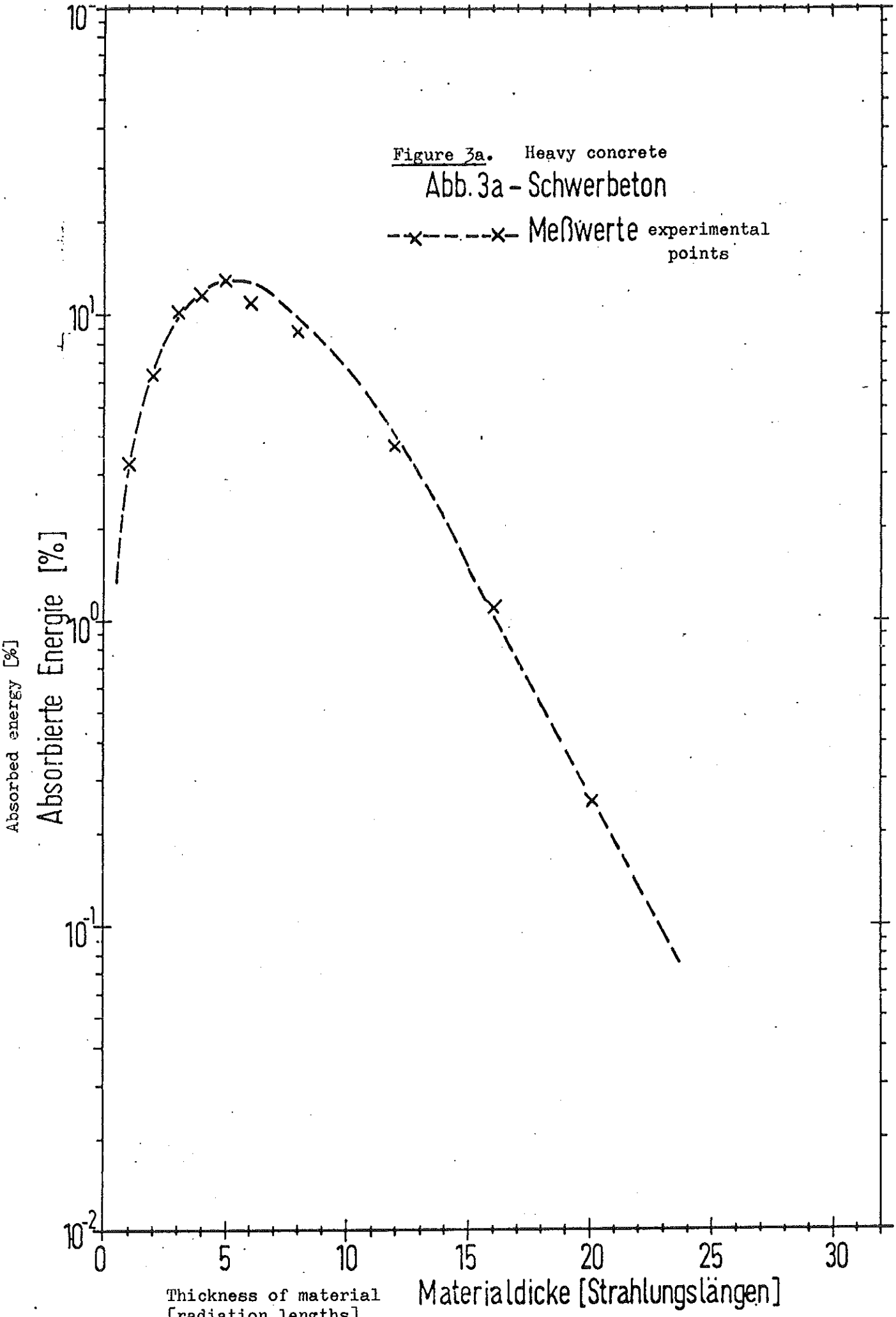

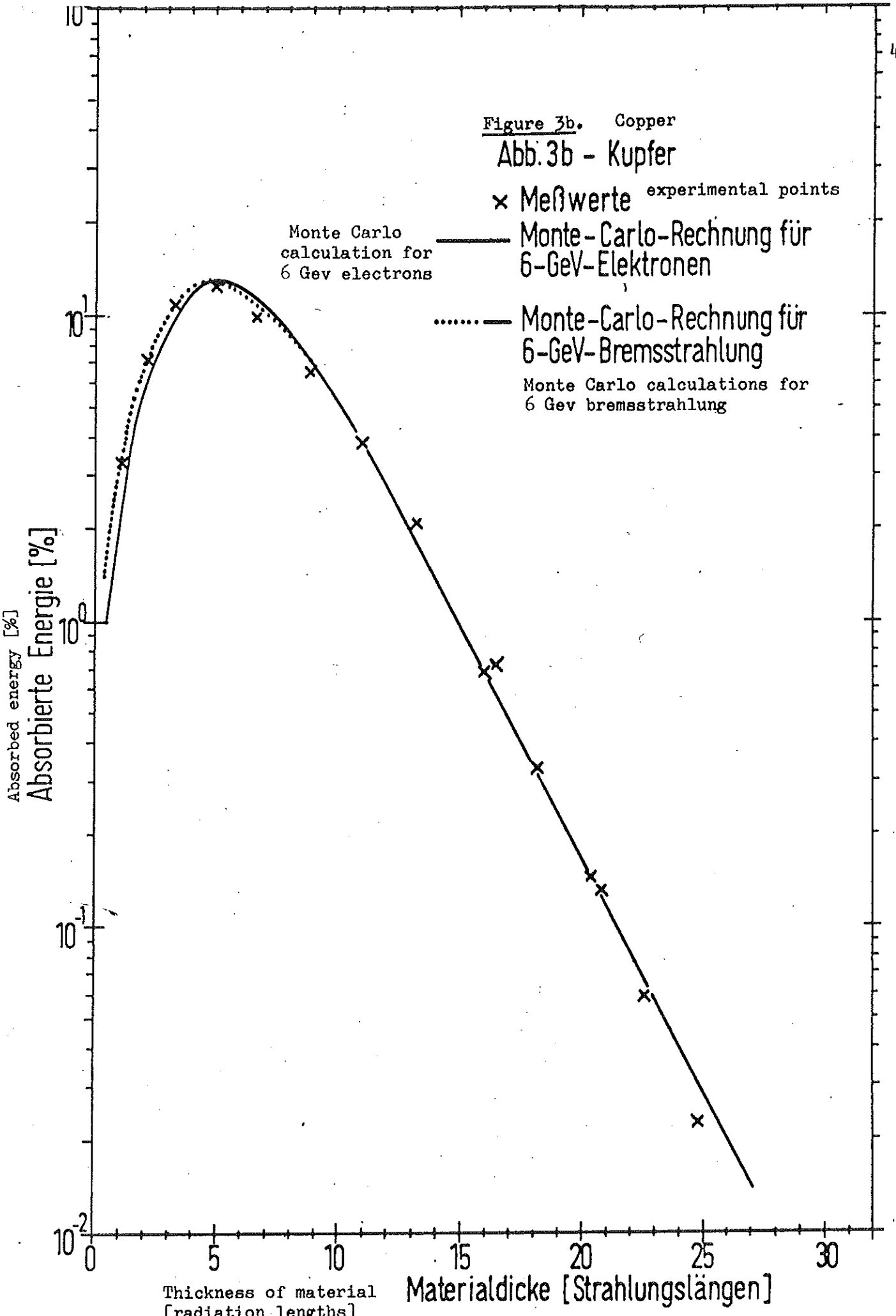


Figure 3b. Copper

Abb. 3b - Kupfer

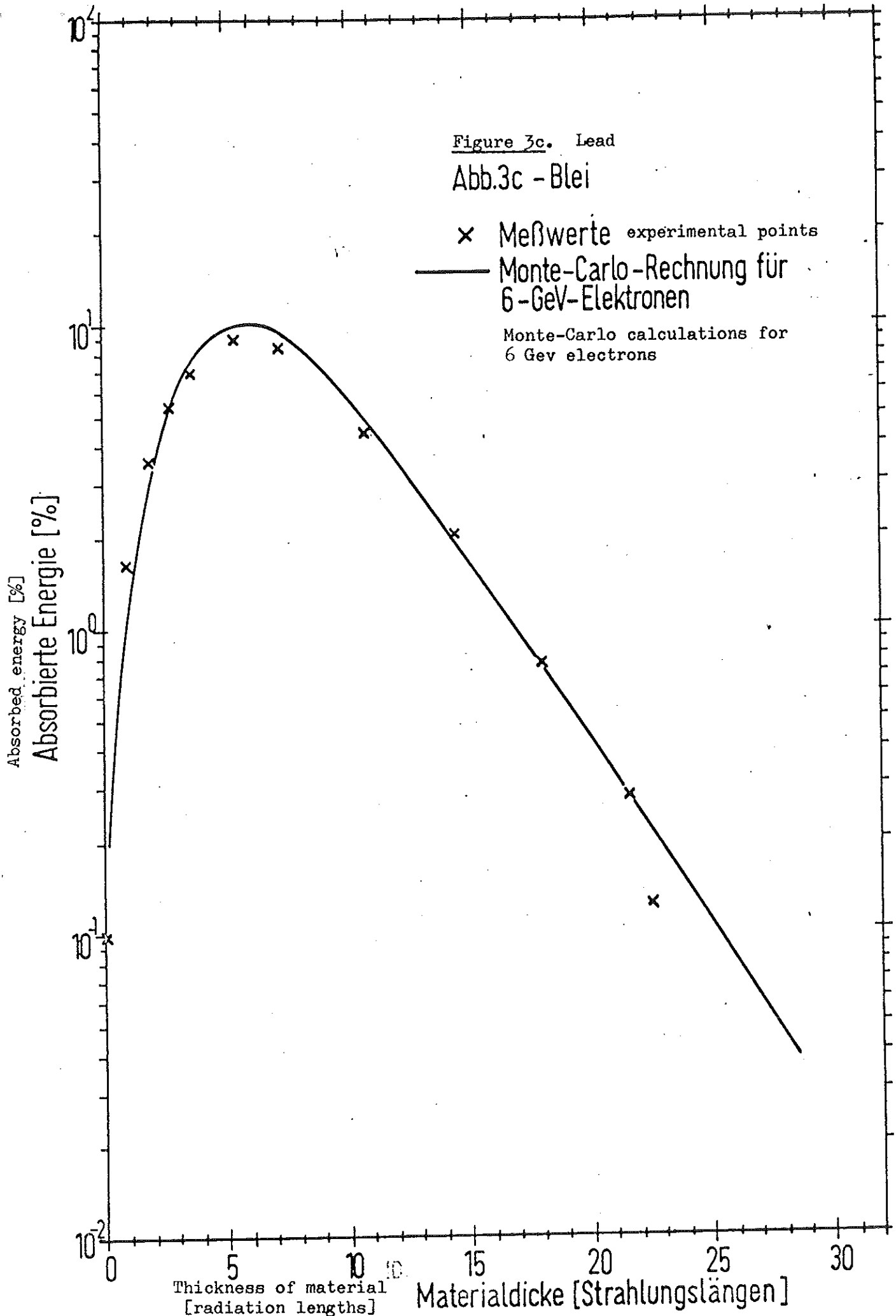


Figure 3c. Lead

Abb.3c - Blei

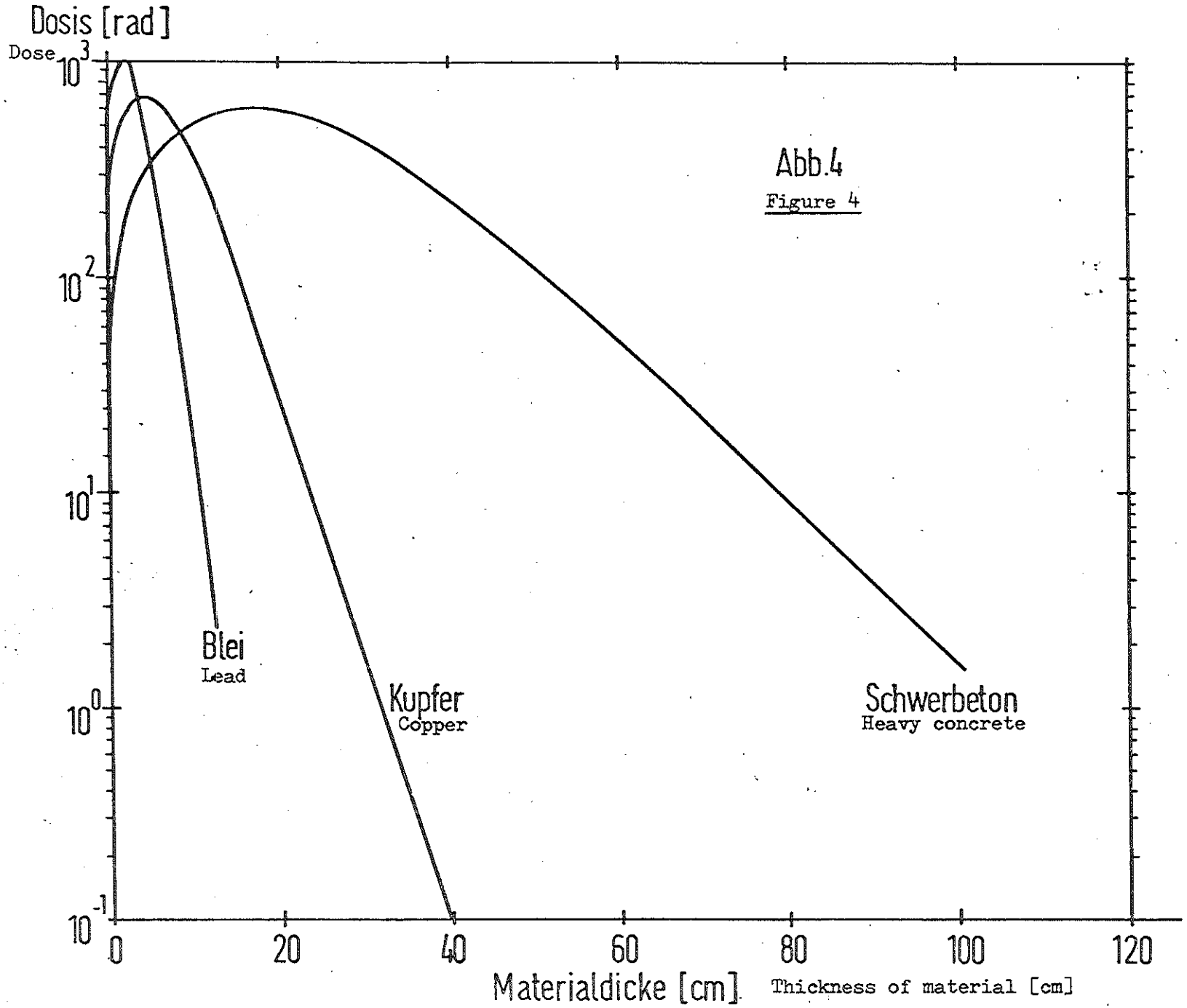


Abb.4

Figure 4

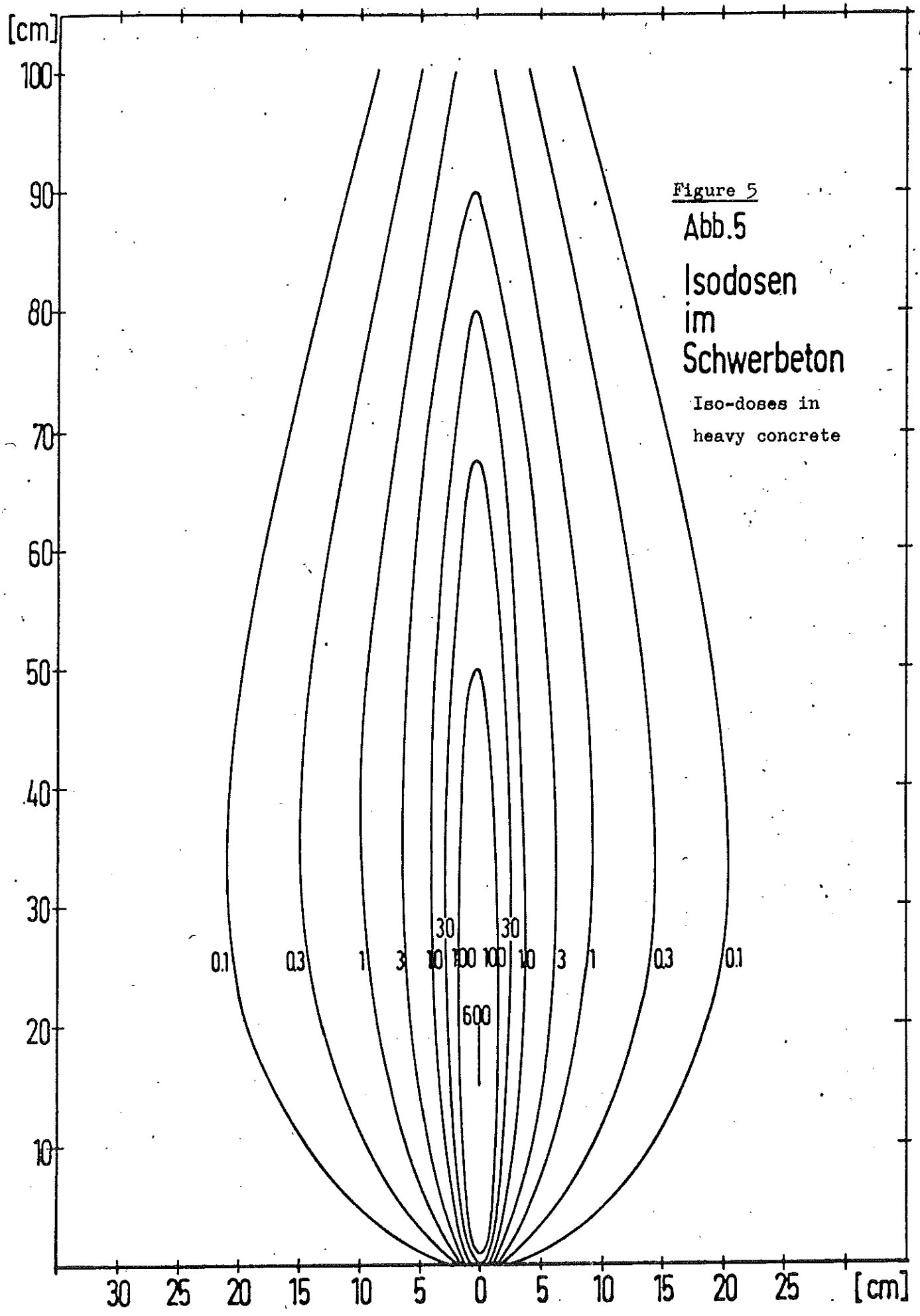


Figure 5

Abb.5

Isodosen im Schwerbeton

Iso-doses in heavy concrete

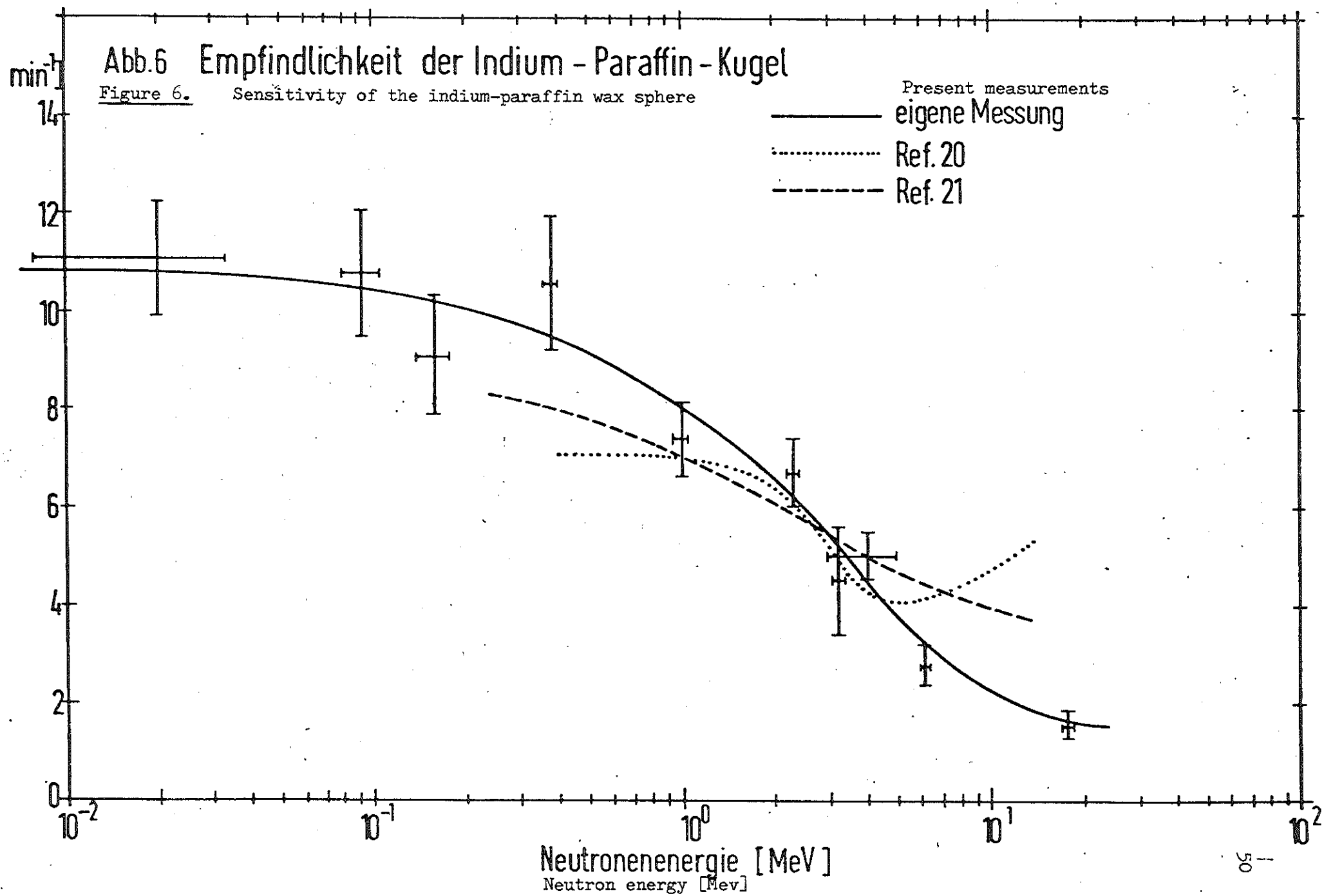
Abb.6 Empfindlichkeit der Indium - Paraffin - Kugel
Figure 6. Sensitivity of the indium-paraffin wax sphere
min⁻¹
Present measurements
eigene Messung
Ref. 20
Ref. 21
14
12
10
8
6
4
2
0
10⁻²
10⁻¹
10⁰
10¹
10²
Neutronenenergie [MeV]
Neutron energy [Mev]

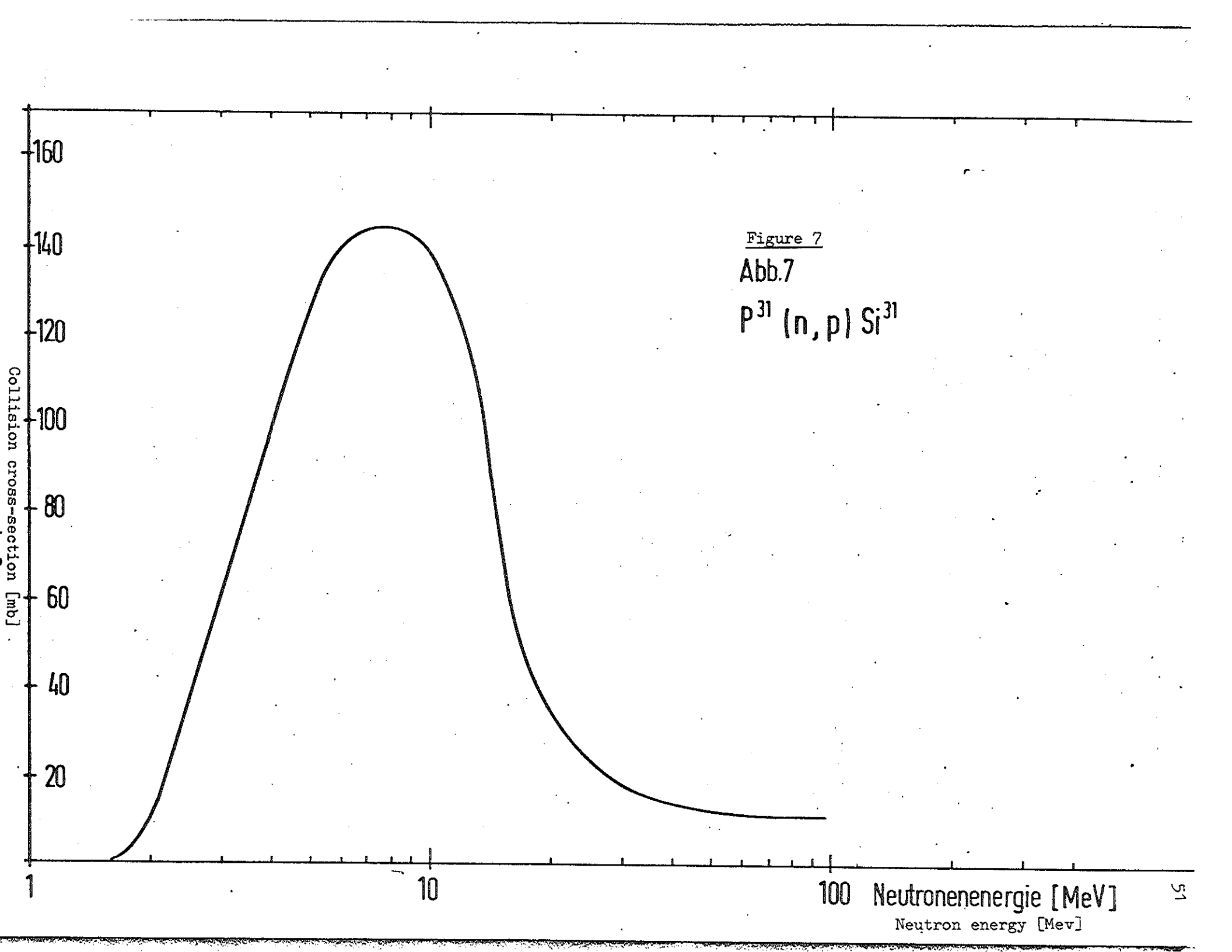


Figure 7

Abb.7

$P^{31}(n,p)Si^{31}$

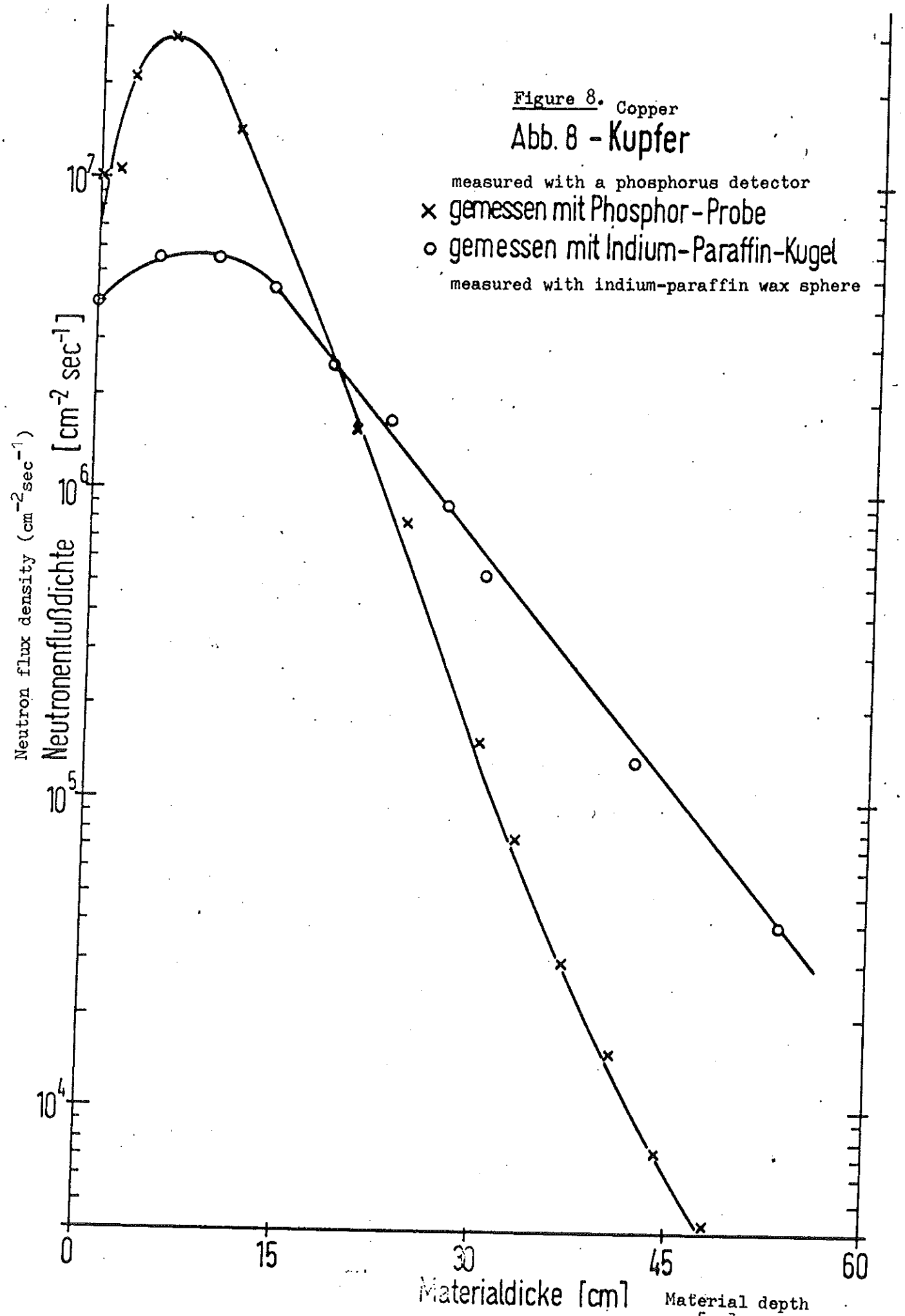
Figure 8. Copper
Abb. 8 - Kupfer
measured with a phosphorus detector
× gemessen mit Phosphor-Probe
o gemessen mit Indium-Paraffin-Kugel
measured with indium-paraffin wax sphere
Neutron flux density (cm⁻²sec⁻¹)
Neutronenflußdichte [cm⁻² sec⁻¹]
10⁷
10⁶
10⁵
10⁴
0
15
30
45
60
Materialdicke [cm]
Material depth

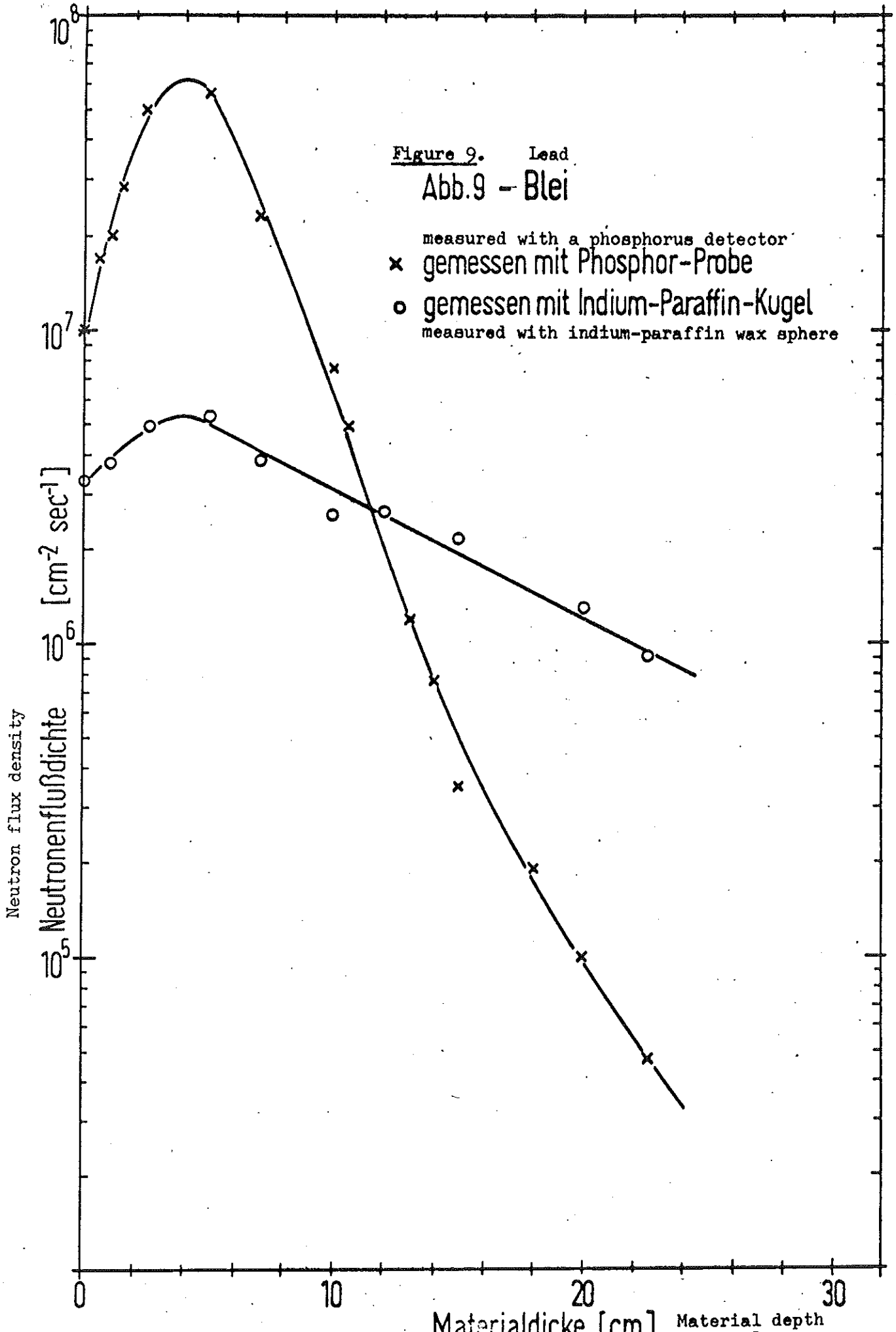
Figure 9. Lead
Abb.9 – Blei
measured with a phosphorus detector
× gemessen mit Phosphor-Probe
o gemessen mit Indium-Paraffin-Kugel
measured with indium-paraffin wax sphere
Neutron flux density
Neutronenflußdichte [cm-2 sec-1]
10^8
10^7
10^6
10^5
0
10
20
30
Materialdicke [cm] Material depth

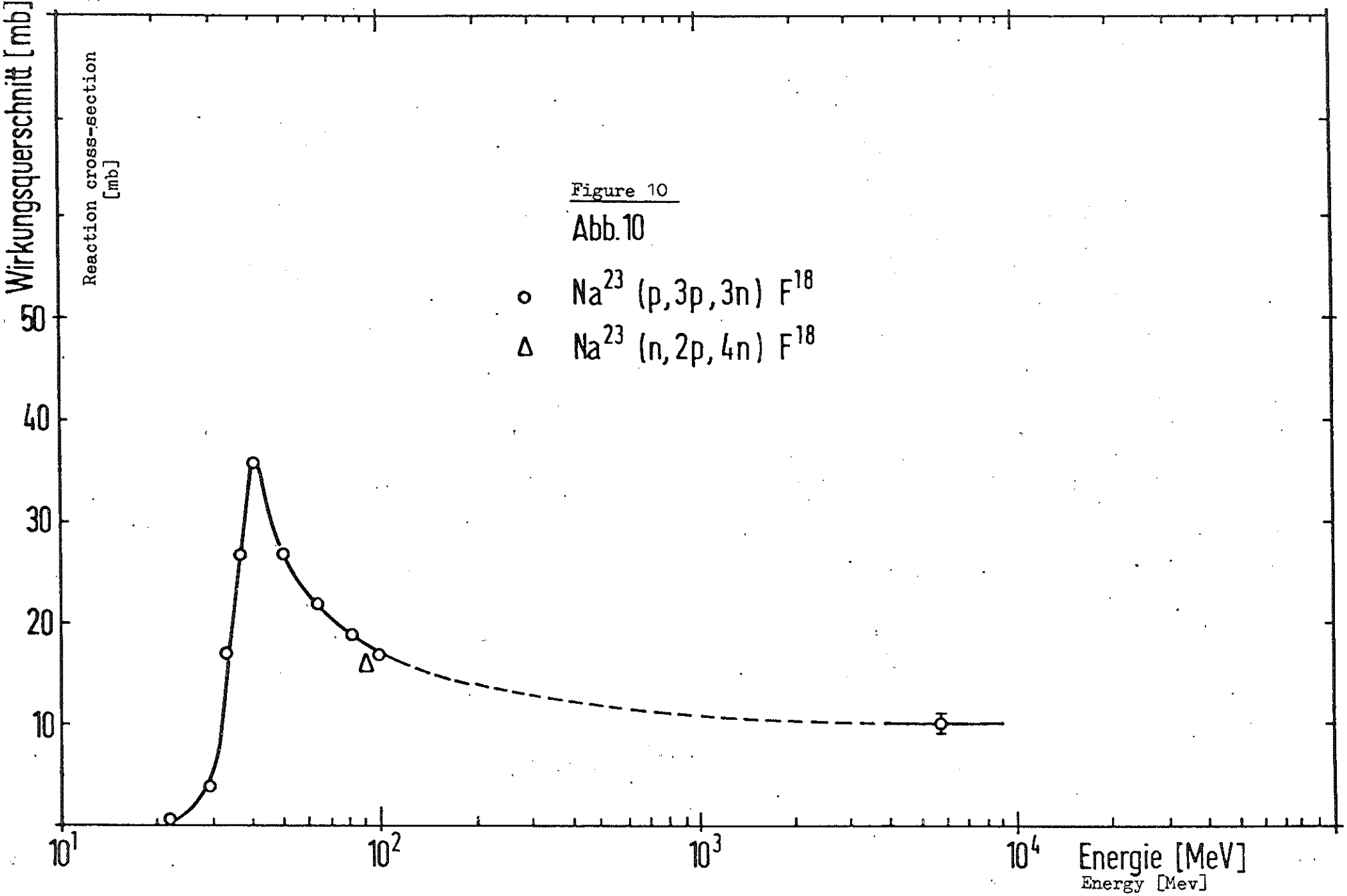


Figure 10

Abb. 10

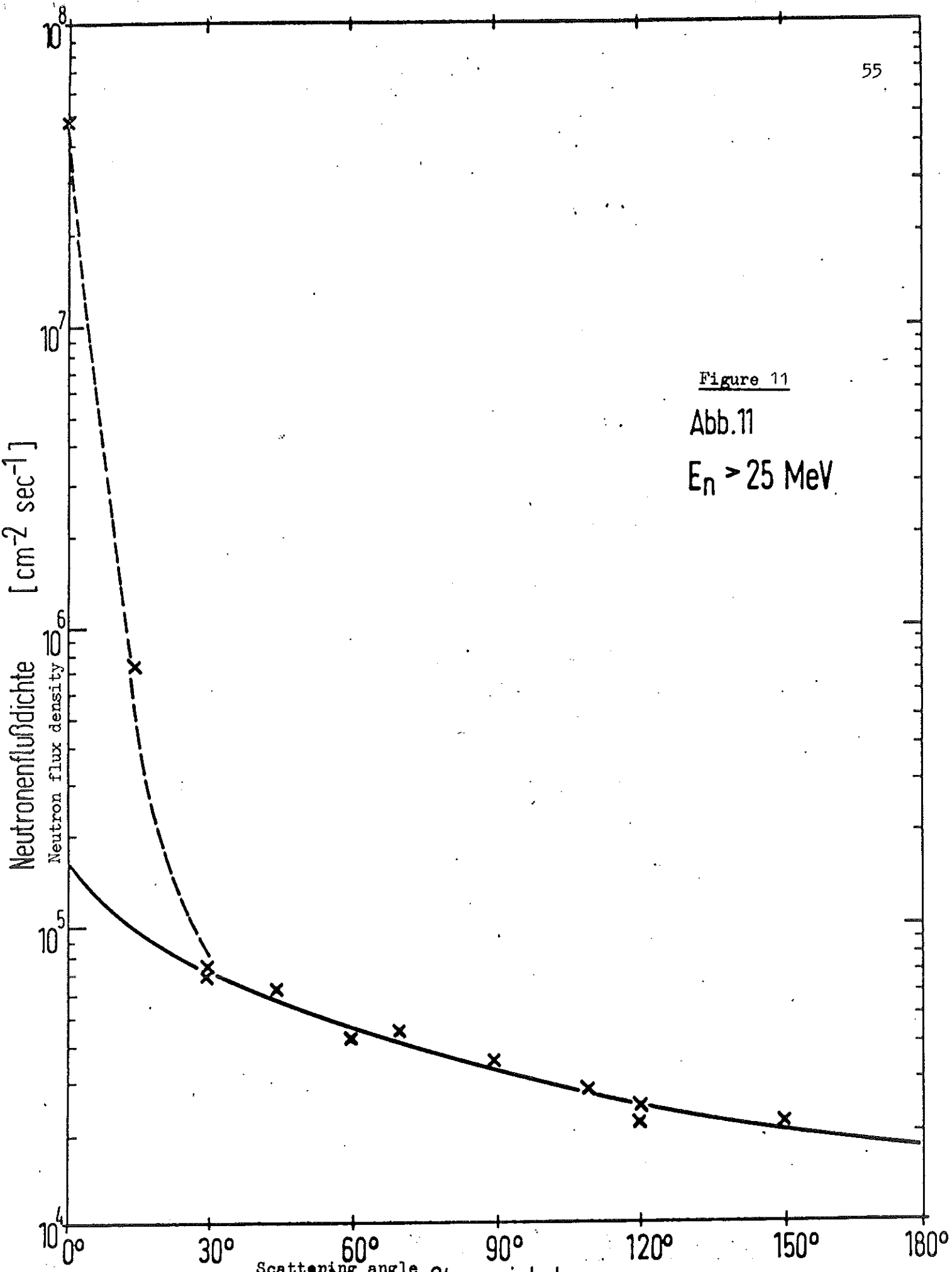


Figure 11

Abb.11

$E_n > 25$ MeV